Remote Sensing of Environment 223 (2019) 50–62

Contents lists available at ScienceDirect

Remote Sensing of Environment

journal homepage: www.elsevier.com/locate/rse

Understanding the relationship between vegetation greenness and productivity across dryland ecosystems through the integration of PhenoCam, satellite, and eddy covariance data

D. Yan[a,*], R.L. Scott[b], D.J.P. Moore[a], J.A. Biederman[b], W.K. Smith[a]

[a] School of Natural Resources and the Environment, University of Arizona, Tucson, AZ 85721, United States of America
[b] Southwest Watershed Research Center, USDA Agricultural Research Service, Tucson, AZ 85719, United States of America

ARTICLE INFO

Keywords:
Drylands
Greenness indices
Gross primary productivity
PhenoCam
Landsat
MODIS

ABSTRACT

Drylands account for approximately 40% of the global land surface and play a dominant role in the trend and variability of terrestrial carbon uptake and storage. Gross ecosystem photosynthesis – termed gross primary productivity (GPP) – is a critical driver of terrestrial carbon uptake and remains challenging to be observed directly. Currently, vegetation indices that largely capture changes in greenness are the most commonly used datasets in satellite-based GPP modeling. However, there remains significant uncertainty in the spatiotemporal relationship between greenness indices and GPP, especially for relatively heterogeneous dryland ecosystems. In this paper, we compared vegetation greenness indices from PhenoCam and satellite (Landsat and MODIS) observations against GPP estimates from the eddy covariance technique, across three representative ecosystem types of the southwestern United States. We systematically evaluated the changes in the relationship between vegetation greenness indices and GPP: i) across spatial scales of canopy-level, 30-meter, and 500-meter resolution; and ii) across temporal scale of daily, 8-day, 16-day, and monthly resolution. We found that greenness-GPP relationships were independent of spatial scales as long as land cover type and composition remained relatively constant. We also found that the greenness-GPP relationships became stronger as the time interval increased, with the strongest relationships observed at the monthly resolution. We posit that the greenness-GPP relationship breaks down at short timescales because greenness changes more slowly than plant physiological function, which responds rapidly to changes in key biophysical drivers. These findings provide insights into the potential for and limitations of modeling GPP using remotely sensed greenness indices across dryland ecosystem types.

1. Introduction

Terrestrial ecosystem carbon uptake dynamics respond to changes in climate and play a critical role in either ameliorating or accelerating the atmospheric CO_2 growth rate (Jung et al., 2017). Drylands – which account for approximately 40% of the global land surface (Reynolds et al., 2007) – have recently been highlighted as dominant in driving both the trend and interannual variability of the net carbon flux in the global terrestrial ecosystems over recent years (Ahlström et al., 2015). Yet, carbon cycling in drylands is less well understood due to a historical lack of long-term carbon exchange measurements. This poor understanding can also be attributed to challenges in modeling carbon exchange in drylands such as the highly variable hydrometeorological conditions, and the mixture of vegetation with different forms (e.g., herbaceous vs. woody) and photosynthetic pathways (e.g., C3, C4 and crassulacean acid metabolism) (Biederman et al., 2017; Smith et al., 2018). Southwestern North America hosts a range of dryland ecosystems such as shrublands, grasslands, and woody plant-encroached grasslands. Woody encroachment has been expected to substantially affect the structure and function of dryland ecosystems in the southwestern United States (Archer et al., 2001; Pacala et al., 2001; Scott et al., 2006a). Globally, shrubland ecosystems alone account for about 35% of the total dryland area (Biederman et al., 2018; Broxton et al., 2014) while the storage of organic carbon in grassland soils is estimated to account for up to 30% of the global soil organic carbon (Derner and Schuman, 2007; Hewins et al., 2018).

Gross photosynthesis – termed gross primary productivity (GPP) – is the major factor controlling terrestrial ecosystem carbon uptake and since it is challenging to directly observe GPP, it must be estimated (Frankenberg et al., 2011; Verma et al., 2014). Remote sensing remains

* Corresponding author.
E-mail address: yand@email.arizona.edu (D. Yan).

https://doi.org/10.1016/j.rse.2018.12.029
Received 26 March 2018; Received in revised form 8 December 2018; Accepted 21 December 2018

the most common way to estimate GPP in a frequent, repeatable and consistent manner from regional to global scales (Frankenberg et al., 2011; Running et al., 2004; Smith et al., 2016). Many current remote sensing models typically quantify GPP using a greenness-based Light Use Efficiency (LUE) approach. For instance, the operational GPP product from the Moderate Resolution Imaging Spectroradiometer (MODIS) is generated by incorporating photosynthetically active radiation (PAR), satellite-derived vegetation greenness indices (VI), and model-derived LUE. In this approach, PAR quantifies the incoming solar energy, VI are used as a proxy of the fraction of PAR absorbed by the vegetation (FAPAR), and LUE represents the conversion efficiency of the absorbed PAR to biomass production (Monteith, 1972; Running et al., 2004; Smith et al., 2016; Zhao et al., 2005). Some remote sensing studies also try to empirically model GPP by relating VI such as the Normalized Difference Vegetation Index (NDVI) and/or the Enhanced Vegetation Index (EVI) to GPP measured using the eddy covariance (EC) technique (Barnes et al., 2017; Rahman et al., 2005; Sims et al., 2006b; Wylie et al., 2003). Yet, a growing body of research has highlighted multiple limitations of these GPP modeling approaches when considering dryland ecosystem types (Verma et al., 2014; Biederman et al., 2017). For example, the MODIS GPP product was found to only explain 20% to 30% of the interannual variation in EC-derived GPP across a diversity of southwestern North American ecosystem types (Biederman et al., 2017). Underestimation of interannual variability by the MODIS GPP product can likely be attributed to multiple factors. For instance, dryland ecosystems are often dominated by drought-tolerant deciduous or evergreen species, for which VI and GPP may decouple during periods of water stress (Biederman et al., 2017; Smith et al., 2018). Further, these models are commonly driven by gridded meteorological products that may fail to capture the high spatiotemporal variability in hydrometeorological conditions across this region due to gaps in surface meteorology observatory networks across drylands (Biederman et al., 2017). Finally, although satellite, airborne and near-surface remote sensing platforms have made VI products available at a wide range of spatial (e.g., from canopy to a few kilometers) and temporal resolutions (e.g., from diurnal to weekly), most previous studies rely on monthly remote sensing products with relatively coarse spatial resolutions (e.g., 1 km) (Biederman et al., 2017; Smith et al., 2018).

There remains a critical need to better understand the VI-GPP relationship at different spatiotemporal scales across dryland ecosystems in particular. In this study, we systematically evaluated VI-GPP relationships across spatiotemporal scales for three representative dryland ecosystems in southern Arizona characterized as a shrubland, a grassland, and a woody-encroached grassland, or savanna, site. We then varied the spatial scale from canopy patches (PhenoCam) to 30m (Landsat) to 500m (MODIS), and we varied the temporal scale from daily to 8-day to 16-day to monthly. Our objective was to provide insights into how best to reduce uncertainty in VI-based estimates of GPP for these key dryland ecosystem types.

2. Study sites

This study focused on three dryland Ameriflux EC sites located in representative semiarid ecosystems in southern Arizona (Scott et al., 2015) (Fig. 1). Specifically, the Santa Rita Mesquite site (SRM: 31.82°N, 110.87°W) located in the Santa Rita Experimental Range, is a semiarid savanna site resulting from velvet mesquite (*Prosopis velutina* Woot.) encroachment into perennial C4 grasslands (i.e., *Digitaria californica* Benth. and *Eragrostis lehmanniana* Nees) (Scott et al., 2009). The other two study sites are the Lucky Hills Shrubland (WHS: 31.74°N, 110.05°W) and Kendall Grassland (WKG: 31.74°N, 109.94°W) located on the Walnut Gulch Experimental Watershed operated by the USDA Agricultural Research Service (Scott et al., 2010). The WHS site is dominated by Chihuahuan Desert shrub species with heights ranging from 0.3 to 1.0 m (Scott et al., 2006b). The WKG site is mainly covered by Lehmann lovegrass (*Eragrostis lehmanniana* Nees) with a small fraction of mesquite and shrub species (Scott et al., 2010).

The three study sites have very similar seasonal patterns of temperature and precipitation (Fig. 2). At SRM for example, during 2004–2016, average monthly temperature varied from between 10 °C and 15 °C during the winter months (December–March) to between 25 °C and 27 °C in summer (July–September). Based on precipitation measured during 2004–2016, the mean annual rainfall was 352 mm, approximately 63% of which occurred during the summer months as a result of the North American monsoon. The winter months represent another relatively wet period, the precipitation during which, however, had higher inter-annual variation than that of summer precipitation. Winter precipitation accounted for approximately 20% of total annual rainfall on average. The spring months (April–June) were the driest period in a year, the rainfall of which only accounted for about 10% of the total annual rainfall. More details of the species composition and the climate characteristics of the study sites can be found in (Scott et al., 2015).

3. Data and methods

3.1. Eddy covariance measurements

Ecosystem CO_2 flux at the study sites was quantified using the eddy covariance technique. Specifically, the wind velocity vector, sonic temperature and CO_2 concentration were measured by three-dimensional, sonic anemometers (CSAT-3; Campbell Scientific) and open-path infrared gas analyzers (LI-7500, LI-COR) with a sampling frequency of 10 Hz. Daily GPP was calculated from these high frequency measurements as described in (Scott et al., 2010, 2009). Since our sites are affiliated with the Ameriflux network (http://ameriflux.lbl.gov/), the instrument configuration and data processing techniques have been further verified against the network's standards. Additional details of the eddy covariance instrument configuration, and the procedures to derive GPP can be found in (Scott et al., 2010, 2009).

3.2. PhenoCam data

PhenoCam imagery was available from 2013 to 2016 at WKG and WHS sites while it was available between 2014 and 2016 at the SRM site. Specifically, half-hourly images of the WKG and WHS sites were captured using a NetCam SC camera with an infrared filter. The NetCam SC camera is able to capture both RGB (filter on) and infrared (filter off) images (Liu et al., 2017; Petach et al., 2014). We downloaded the RGB and infrared images for the WKG and WHS sites from the PhenoCam Network via: https://phenocam.sr.unh.edu/webcam/network/download/ (Milliman et al., 2018). In contrast, PhenoCam imagery of the SRM site consisted of hourly RGB-only images captured using a Canon PowerShot D20 camera. Efforts are underway to get the SRM site and the available historical data into the PhenoCam Network.

We used the functions implemented in the R package “phenopix” (Filippa et al., 2016; Petach et al., 2014) to extract time series of NDVI at WKG and WHS, and Green Chromatic Coordinate (GCC) time series at SRM. Specifically, we first used the function *DrawROI()* to delineate the Region-Of-Interest (ROI) for each site (Fig. 3). The considerations for determining the particular ROIs in Fig. 3d–f along with the descriptions of how these ROIs were used to evaluate the view angle effects in greenness indices derived from PhenoCam imagery are provided in Section 3.5.2. We then used the function *ExractVIs()* to calculate GCC on a per-pixel basis by dividing the digital number from the green channel by the sum of digital number from red, green and blue channels (Toomey et al., 2015), which is the same method utilized to calculate GCC in the standard PhenoCam dataset (Richardson et al., 2018). NDVI was calculated using the function *NDVI()* in the “phenopix” package. The details of integrating RGB and infrared images to calculate NDVI on a per-pixel basis can be found in (Liu et al., 2017;

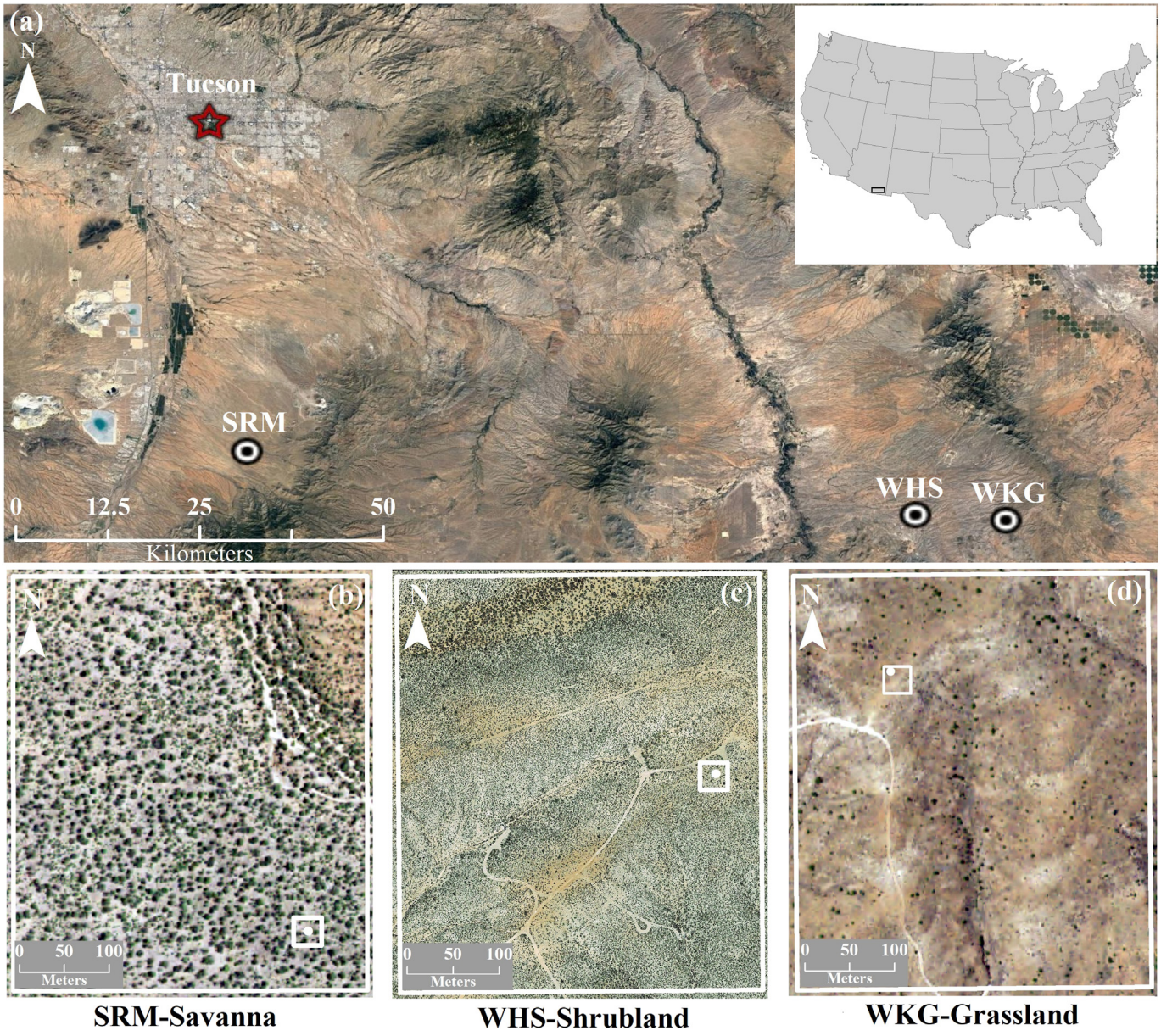

Fig. 1. The location and land cover of the study sites in southern Arizona: (a) Locations of the study sites in southern Arizona overlaid on Landsat images from Google Earth; (b–d) high-resolution imagery of the three study sites. Detailed information of the characteristics of the high-resolution imagery is presented in Supplemental Table S1. The large and small white box represents the boundary of a 500-m MODIS and 30-m Landsat pixel, respectively. The white dots indicate the locations of PhenoCam/eddy covariance towers.

Petach et al., 2014). Note that PhenoCam-derived NDVI can have negative values, which resulted from the fact that NDVI was calculated using digital numbers from PhenoCam imagery instead of spectral reflectance (Liu et al., 2017; Petach et al., 2014). Since we are only interested in the seasonal pattern of VI rather than its magnitude, we did not apply the method proposed by (Petach et al., 2014) to scale PhenoCam NDVI to the same range of NDVI derived from satellite data (details available in Section 3.3). We also point out that potential impacts of changing image exposure on the extraction of greenness from PhenoCam imagery were accounted for in the R package "Phenopix" by normalizing the digital numbers of any given image against the image exposure of the same image. NDVI and GCC calculated in this way have been shown to have strong agreements with those derived from ground spectral sensors (Petach et al., 2014) and MODIS (Filippa et al., 2018). The main features and applications of the "phenopix" package are documented in Filippa et al. (2016). The full descriptions of the functions used in this study can be found in the "phenopix" package manual, which can be accessed via: https://cran.r-project.org/web/packages/phenopix/phenopix.pdf. NDVI and GCC are hereafter referred to as VI. The VI for a given ROI was calculated as the average VI from the enclosed pixels. Daily VI for a given ROI was determined as the median of the VI calculated using images captured during 8:00–17:00. In order to minimize the day-to-day VI changes caused by the changes in illumination conditions, we further employed the commonly used local polynomial regression fitting (Browning et al., 2017; Sonnentag et al., 2012) to smooth the daily VI time series.

3.3. Satellite data

We downloaded 16-day, 30-m Landsat-8 Operational Land Imager surface reflectance (SR), and the associated Quality Assurance (QA) data from the Science Processing Architecture of USGS Earth Resources Observation and Science Center: https://espa.cr.usgs.gov/. We also downloaded daily, 500-m MODIS SR and QA (MCD43A4) (Schaaf and

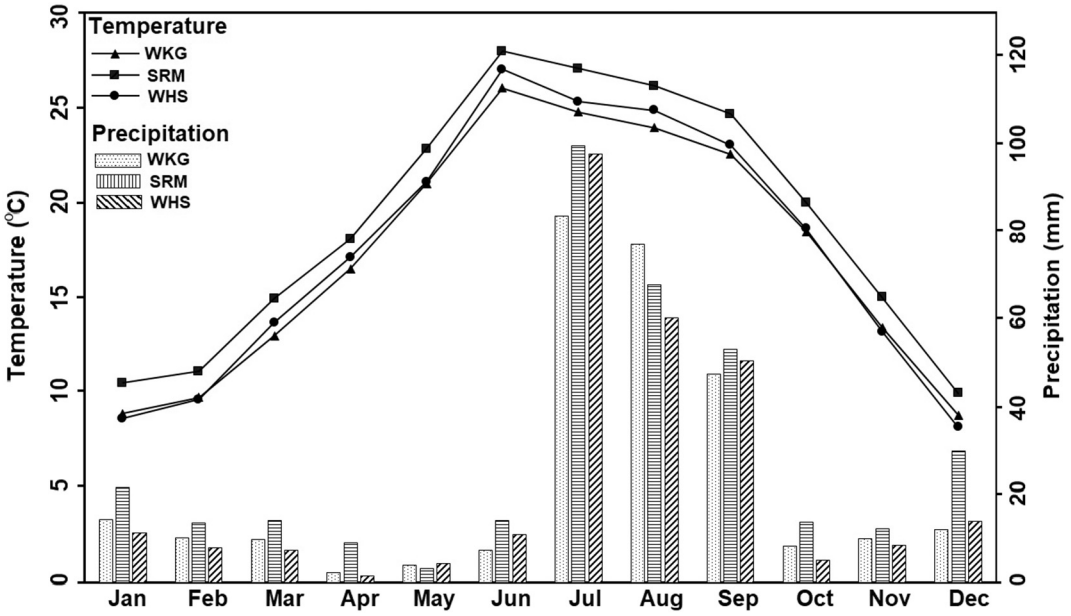

Fig. 2. The long-term average monthly temperature (left y-axis, dotted lines) and precipitation (right y-axis, bars) of the study sites during 2004–2016. More details of the instrument setup for temperature and precipitation measurements at the three sites can be found in two relevant studies (Scott, 2010; Scott et al., 2009).

Wang, 2015) using the MODIS Collection 6 Global Subsetting Tool provided by the Oak Ridge National Laboratory Distributed Active Archive Center (DAAC, 2017). The Collection 6 MCD43A4 product is generated daily based on BRDF parameters retrieved over a 16-day period (Schaaf and Wang, 2015). For each site, we calculated the corresponding VI (i.e., NDVI at WKG and WHS, and GCC at SRM) for each Landsat/MODIS pixel, the centroid of which fell in the 1 km-radius tower footprint (i.e., approximately 3500 Landsat and 17 MODIS pixels, respectively). We hereafter used "footprint scale" to denote the area inside a 1 km-radius circle around the tower, an area that roughly encompasses the source region for the measured tower fluxes. MODIS/Landsat GCC was calculated based on surface reflectance from red, green and blue bands (Hufkens et al., 2012). For each 30-m Landsat pixel, we further converted the 16-day VI time series to an 8-day time series by interpolating the mid-point VI between two consecutive 16-day VI. The mid-point VI was calculated as the average of the two 16-day VI only when both of them had good quality (i.e., cloud-free and without sensor saturation). In other words, the mid-point VI was not calculated if either of the two neighboring 16-day VIs was not of good quality.

3.4. Land cover classification

We conducted land cover classifications using both unsupervised and supervised classification algorithms implemented in the ENVI image processing software to understand how the land cover composition varied across spatial scales at each site. The target land cover category was mesquite shrubs, grasses and bare soil for WKG and SRM, while it became shrubs and bare soil at WHS. The land cover classification within the delineated PhenoCam ROIs (i.e., (a)–(c) in Fig. 3) were carried out using the ISODATA unsupervised classification algorithm. Specifically, we first used the ISODATA classifier to determine 10 potential land cover classes for the PhenoCam ROI at each site. We then manually grouped the 10 potential classes into the target land cover categories at each site. Finally, we manually corrected any wrong classifications by comparing the grouped land cover classes with the original PhenoCam imagery. The land cover within the 1 km-radius tower footprint was determined by classifying high-resolution imagery (i.e., (b)–(d) in Fig. 1) using the maximum likelihood supervised classification algorithm. Specifically, for WKG and SRM, we used the 1 m 4-band aerial imagery acquired by the USDA National Agriculture Imagery Program (NAIP) on June 21st and July 2nd of 2015, respectively. We downloaded the NAIP imagery by adding the following link: https://gis.apfo.usda.gov/arcgis//rest/services to the Web Mapping Services provided by the ESRI ArcGIS Desktop Application. For WHS, since shrub and bare soil were not visually distinct from each other in the NAIP imagery, we used a high-resolution image downloaded from the historical imagery archive provided by Google Earth Pro (image acquisition date: April 6th, 2013). A complete list of the characteristics of the high-resolution imagery acquired for the study sites is presented in Supplemental Table S1.

3.5. Quantifying the changes in VI-GPP relationship across spatial and temporal scales

We quantified changes in VI-GPP relationship across spatial and temporal scales using statistics retrieved from linear regression analyses, in which VI and GPP were used as the predictor and response variables, respectively. For each regression, we retrieved the following statistics: the coefficient-of-determination (R^2), the total absolute residual (Δ), the Root-Mean-Square-Difference (RMSD) and the p value. Specifically, Δ and RMSD were calculated using the following equations.

$$\Delta = \sum_{i=1}^{N} |GPP_i - \overline{GPP_i}| \quad (1)$$

$$\mathrm{RMSD} = \sqrt{\frac{\sum_{i=1}^{N} (GPP_i - \overline{GPP_i})^2}{N}} \quad (2)$$

where, GPP_i and $\overline{GPP_i}$ refer to the measured and predicted GPP, respectively. N is the total number of samples.

3.5.1. Characterizing changes in VI-GPP relationship across spatial scales

We compared the statistics from the regressions in which VI from PhenoCam, Landsat and MODIS were used separately as the predictor variable against the same response variable, which is the GPP derived from eddy covariance measurements as described in Section 3.1. Specifically, PhenoCam VI were computed based on ROIs in Fig. 3a–c. Satellite VI were extracted from the 30-m/500-m pixel in which the

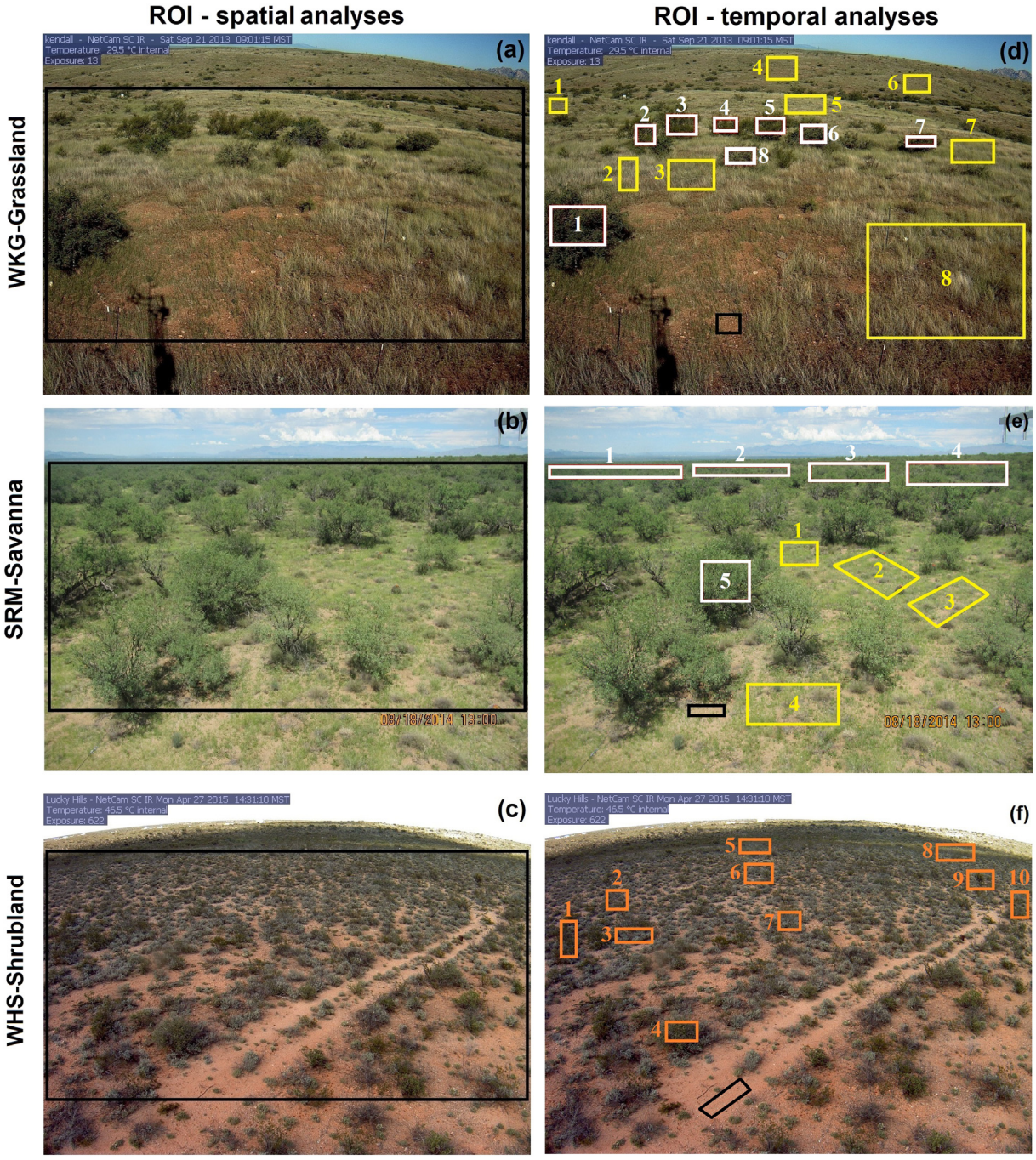

Fig. 3. PhenoCam views with the delineated Region-of-Interest (ROI). (a)–(c): the single ROI used to extract VI time series in the spatial analyses; (d)–(f): ROI delineated to extract VI time series from major land cover types in the temporal analyses. Black boxes in (d)–(f) represent ROIs delineated for bare soil. White and yellow boxes in (d) and (e) indicate ROIs delineated for mesquite and grass, respectively. Orange boxes in (f) indicate ROIs delineated for shrub. (For interpretation of the references to color in this figure legend, the reader is referred to the web version of this article.)

eddy covariance tower is located. Note that we only used the VI from the days on which PhenoCam observations were available, and both Landsat and MODIS had good quality observations. Therefore, there were equal numbers of samples in the three regressions at any given site.

3.5.2. Characterizing changes VI-GPP relationship across temporal scales

We scaled VI from PhenoCam, Landsat and MODIS to the 1 km-radius tower footprint (Schmid, 2002; Sims et al., 2006b) so that variations in VI-GPP relationship with temporal scales are comparable across sensors. Satellite VI at the tower footprint scale was calculated as the average VI from good quality pixels within the 1 km-radius tower footprint. We followed the procedures proposed by (Liu et al., 2017) to upscale PhenoCam VI. Specifically, we first delineated separate ROIs (i.e., Fig. 3d–f) targeting major land cover types described in Section 3.4. We determined the positions of the ROIs in Fig. 3d–f with the following considerations. For any given land cover, ROIs should be placed on this land cover at different positions to account for the variability in greenness within PhenoCam's field-of-view. ROIs should be placed at the positions without significant land cover change (e.g., grass dominated in one year and bare soil dominated in another). We then generated daily VI time series for each ROI using the methods

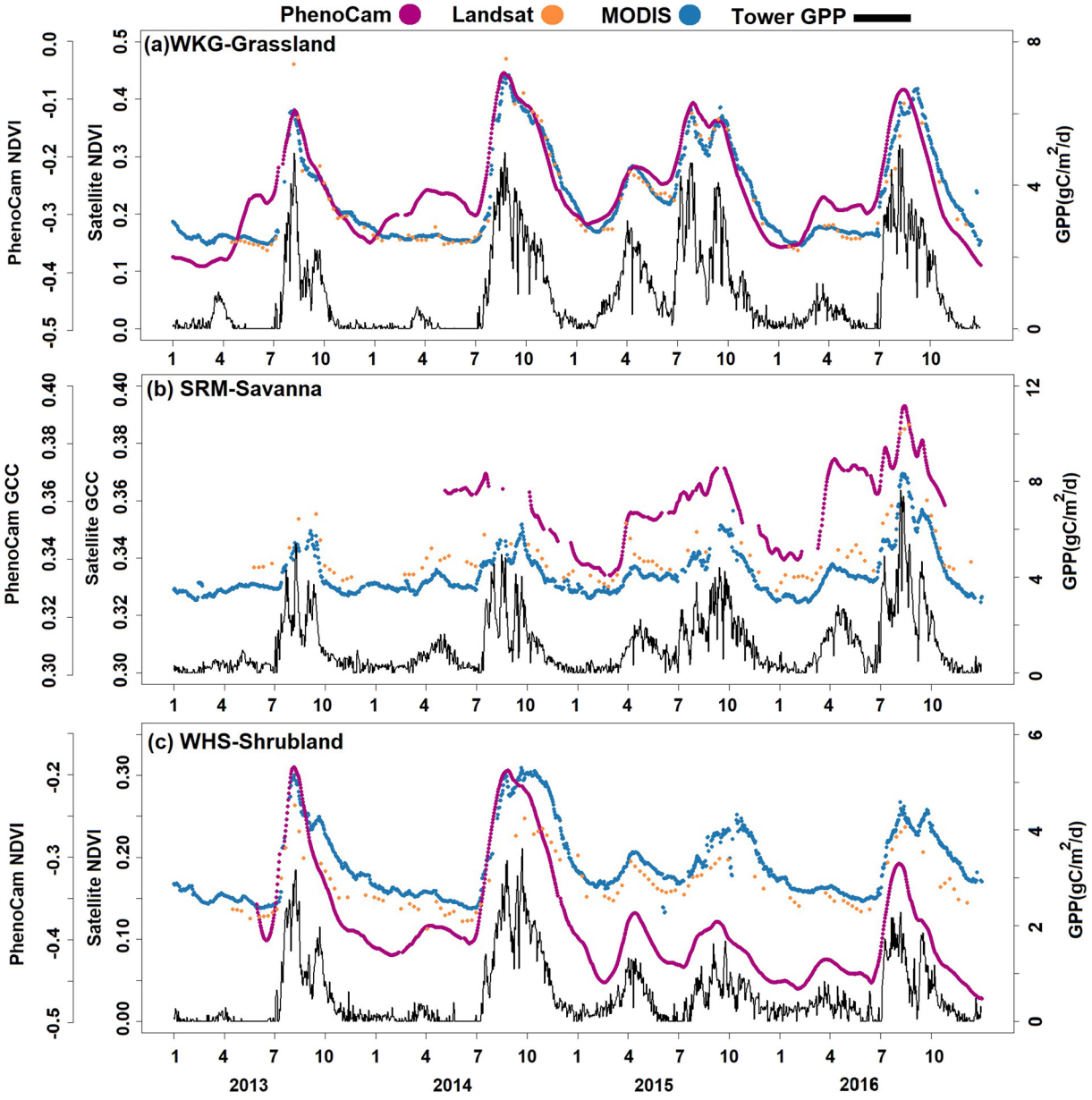

Fig. 4. The VI (left y-axis) and GPP (right y-axis) time series during 2013–2016 at the study sites. Purple, orange and blue dots represent VI from PhenoCam, Landsat and MODIS, respectively, while GPP is shown as solid black lines. Note that GCC was calculated for the SRM site while NDVI was calculated at the WKG and WHS sites. (For interpretation of the references to color in this figure legend, the reader is referred to the web version of this article.)

described in Section 3.2. We further generated an average daily VI time series for each major land cover type based on the associated ROIs. This is to capture the within-class variability in PhenoCam's field-of-view. Note that we found substantial increases in the VI time series extracted from the bare soil ROIs. These greenness increases occurred under two types of conditions. First, the expansion of green leaf area in grass/shrub patches during the monsoon season could result in the extension of green leaves into adjacent bare soil ROIs. Second, some bare soil ROIs can be free of grass/shrub in one year yet partially covered by grass/shrub in another year. In order to remove the greenness increases, we first delineated a single bare soil ROI that was least affected by these two types of conditions for each site (black boxes in Fig. 3d–f). We also identified the time periods during which this bare soil ROI was free of grass/shrub. We then calculated a fixed VI for this bare soil ROI as the mean VI during the time periods when it was free of grass/shrub. The fixed soil VI calculated for WKG, WHS and SRM was −0.40, −0.51 and 0.33, respectively. Finally, the footprint scale PhenoCam VI was determined as the average VI of the major land cover types weighted by their corresponding proportion in the 1 km-radius tower footprint, which was derived from the land cover classification using aerial imagery described in Section 3.4. We then conducted a series of regression analyses based on GPP and footprint scale VI at daily, 8-day, 16-day and monthly intervals. Note that since daily Landsat data are unavailable, the regression analyses at daily scale were omitted for Landsat. Daily GPP derived from eddy covariance measurements were temporally aggregated to a specific temporal scale by determining the mean value during the corresponding aggregation period. The footprint scale VI was temporally aggregated in the same manner. We hereafter referred to these regression analyses using the mean VI and GPP as the original temporal regression analyses.

We conducted two additional analyses to address the issues that could confound the temporal scale analysis: the changes in the sample size caused by temporal aggregation and the view angle effects on VI extracted from different PhenoCam ROIs. Since temporal aggregation

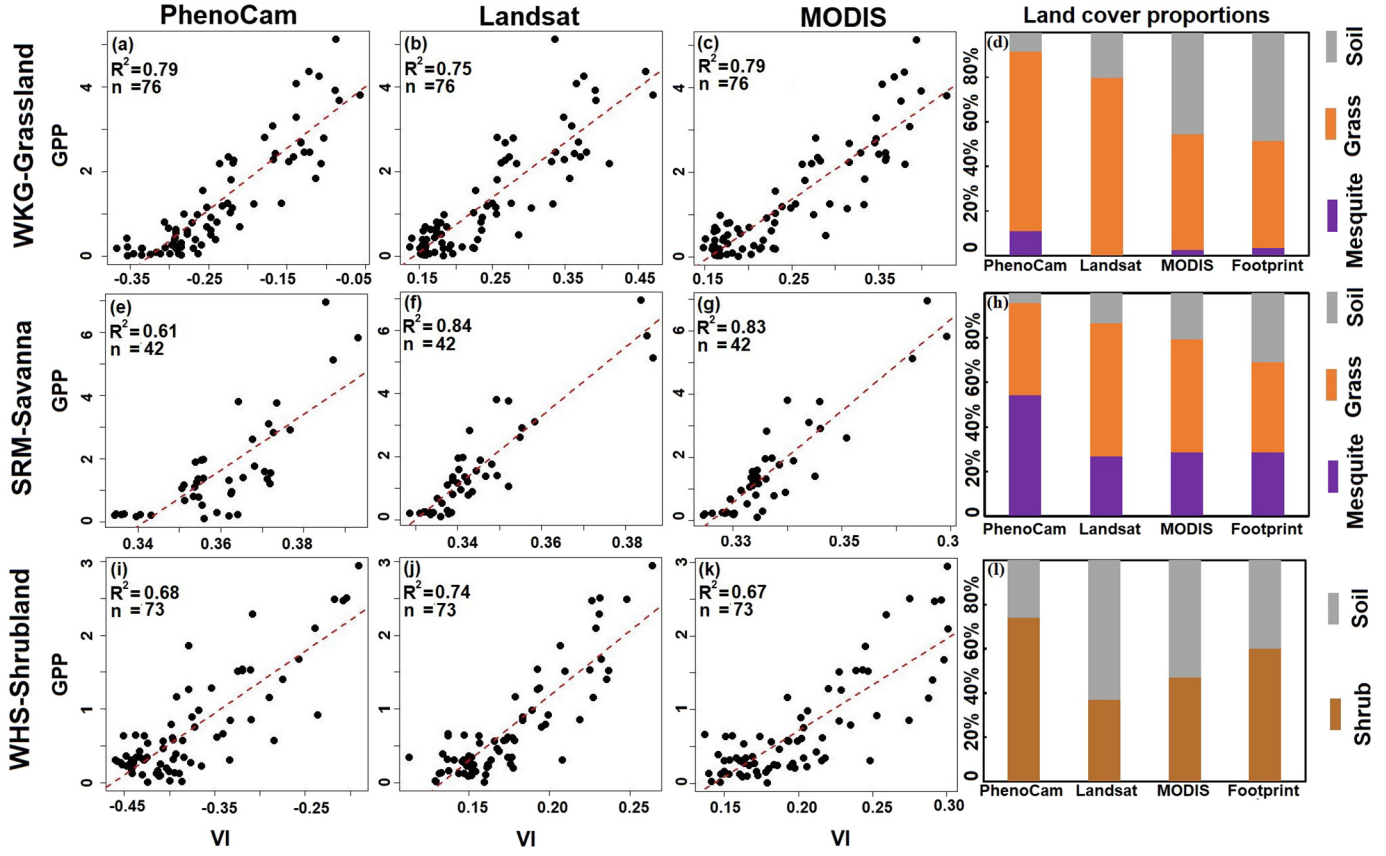

Fig. 5. Changes in VI-GPP relationship across spatial scales (i.e., PhenoCam: canopy, Landsat: 30-m, MODIS: 500-m) (column 1–3 from the left), and the land cover proportions (the right-most bar plot). In the scatterplots, the x-axis and y-axis is VI and GPP, respectively. VI and GPP shown in this figure were extracted from daily time series. R^2 and the number of samples used (n) are reported at the upper left corner of the scatter plots. Red dashed lines are the fitted regression lines. For each bar in the bar plots (d) and (h), the top, center and bottom portion of the bar represents the proportion of soil (gray), grass (orange) and mesquite (purple), respectively. For each bar in the bar plot (l) the upper and lower portion of the bar represents the proportion of soil and shrub, respectively. (For interpretation of the references to color in this figure legend, the reader is referred to the web version of this article.)

inherently reduced the number of samples in a time series, we utilized additional statistical techniques to determine its impact on model performance. Specifically, for each VI and GPP time series at a given site (i.e., daily, 8-day and 16-day), we generated 100 unique time series of the same length (equivalent to the length of monthly time series at the same site) by randomly drawing from the original time series. We then conducted a regression analysis using each of the simulated VI and GPP time series. We then calculated the mean and standard deviation of R^2 across the 100 regression analyses. This additional statistical technique was utilized to control for the potential impacts from changes in sample size and thus ensure that we were testing in isolation the impacts of temporal aggregation on the relationship between VI and GPP. The idea was that if the variation in the mean R^2 generated using the simulated time series from daily to 16-day is consistent with those generated using the original time series, then the possible impacts from changes in sample size can be eliminated.

Although both NDVI and GCC are normalized indices, results from previous studies have shown the angular effects in normalized indices such as NDVI (Gamon, 2015; Sims et al., 2006a; Tian et al., 2010). Therefore, we used the WKG grassland as the test site to determine if using VI extracted from ROIs with substantially different view angles would affect the variations in VI-GPP relationship across temporal scales. Specifically, we first selected two ROIs with substantially different view angles for both mesquite (ROI #1 and #7 in Fig. 3d) and grass (ROI #1 and #8 in Fig. 3d). We calculated the correlation coefficient between daily VI extracted from mesquite ROI #1 and #7 as well as the correlation coefficient between daily VI extracted from grass ROI #1 and #8. We generated four daily PhenoCam VI time series at the footprint scale based on the fixed soil VI at WKG (i.e., −0.4), and the different combinations of mesquite and grass VI from the selected ROIs. We conducted the regression analyses between GPP, and each of the four footprint scale PhenoCam VI time series at daily, 8-day, 16-day and monthly intervals. Finally, we examined if the changes in R^2 across temporal scales derived from the PhenoCam VI generated based on a given combination of selected mesquite and grass ROIs are consistent with those derived from the footprint scale PhenoCam VI generated using VI from all mesquite and grass ROIs in Fig. 3d. Note that although the mesquite and grass ROIs we selected at the WKG site have different view angles, they do not span the full range of the view angles in the PhenoCam imagery (Fig. 3d). Therefore, our test is not thorough in terms of evaluating the view angle effects in the absolute VI values extracted from PhenoCam imagery.

4. Results

4.1. Changes in VI-GPP relationship across spatial scales

The VI and GPP time series during 2013–2016 are presented in Fig. 4. The day-to-day variation in the time series of GPP was higher than that in the VI time series. The consistency in temporal dynamics between PhenoCam and satellite VI, and between VI and GPP was relatively high at the WHS shrubland site. At the WKG grassland and the SRM savanna sites, the consistency in temporal dynamics between VI from different sensors as well as between VI and GPP was higher during summer than that in spring. At the SRM savanna site, for instance, GPP had two peaks with the minor peak in spring and the major peak in

summer during 2014–2016. Both PhenoCam and satellite VI were able to capture the summer peak. During spring, however, while satellite VI was generally coupled with changes in GPP, the temporal dynamics of PhenoCam VI was only consistent with that of GPP during late March and early April but then maintained a plateau despite the declining GPP as spring soil moisture is exhausted by the dry and hot pre-monsoon season (Barron-Gafford et al., 2017; Scott et al., 2008).

Results of the land cover classification within PhenoCam ROIs are presented in Supplemental Fig. S1. The classified NAIP imagery is shown in Supplemental Fig. S2 and the associated accuracy assessment results are summarized in Supplemental Table S2. The overall classification accuracy and the kappa coefficient were all above 95% and 0.90, respectively, at the three sites. The land cover proportions at different spatial scales are reported in the bar plots of Fig. 5. Grass was the dominant land cover across spatial scales at the WKG grassland site. In contrast, at the SRM savanna site, while mesquite dominated the PhenoCam ROI, grass was the dominant land cover within the Landsat/MODIS pixel and tower footprint. At the WHS shrubland site, shrub was the dominant land cover within the PhenoCam ROI and the tower footprint. Bare soil dominated the Landsat pixel and it had a slightly higher proportion than that of shrub within the MODIS pixel.

The regression statistics (i.e., R^2, Δ and RMSD) are summarized in Supplemental Table S3, and the VI-GPP scatter plots are presented in Fig. 5. All the regressions shown in Fig. 5 were highly significant ($p < 0.01$). The biggest change in regression statistics across spatial scales was found at SRM. For instance, R^2 increased by 0.22 (36%) when the spatial scale varied from PhenoCam to satellite at SRM while the R^2 remained relatively consistent across spatial scales at WKG and WHS. The greatest variations in Δ and RMSD across spatial scales were also associated with SRM (Supplemental Table S3).

4.2. Changes in VI-GPP relationship across temporal scales

The time series of mean PhenoCam VI determined based on individual ROIs of major land cover types (i.e., Fig. 3d–f) are presented along with tower GPP in Fig. 6. The PhenoCam VI time series for each non-soil ROIs shown in Fig. 3d–f is presented in Supplemental Figs. S3–S5. The consistency in temporal dynamics between VI from mesquite and grass, and between VI and GPP at the grassland site WKG and the savanna site SRM varied between seasons and sites. Specifically, at WKG, the first green-up of mesquite occurred in April followed by a stronger one in July (Fig. 6a). The timings of mesquite green-up at SRM were similar to that at WKG. Unlike WKG, however, the magnitude of the spring green-up at SRM was similar to or even slight higher than that of the summer green-up. In contrast, the green-up of grass at WKG and SRM mainly occurred in July. At WKG and SRM sites, greenness from mesquite and grass approached an annual minimum during winter due to the leaf shedding of mesquite trees and the browning of grasses, respectively. While the timing of annual minimum was similar between mesquite and grass at WKG, a mesquite minimum occurred later than the grass minimum at SRM. Therefore, at both WKG and SRM, mesquite had a longer growing season than that of grass. At WKG, while grass VI corresponded better with GPP than did mesquite VI during spring, both the temporal dynamics of mesquite and grass VI had a relatively high consistency with that of GPP during summer. In contrast, at SRM, the temporal dynamics of mesquite VI was more consistent with that of GPP in spring, and the temporal dynamics of grass VI was more consistent with that of summer GPP. Shrub VI at the WHS shrubland site generally corresponded well in GPP except during late summer when VI exhibited relatively stable decreases while GPP showed strong fluctuation.

The footprint scale PhenoCam and satellite VI along with GPP are shown in Fig. 7. Compared with the VI extracted from a single ROI/pixel in Fig. 4, scaling VI to the tower footprint generally increased the correlation between Landsat and MODIS VI. Compared with WKG and WHS, however, the correlation between Landsat and MODIS VI at SRM was relatively low (Supplemental Fig. S6). The variations in the R^2 across temporal scales are presented in Fig. 8 and the regression scatter plots are presented in Supplemental Figs. S7–S9 (all the regressions were significant with $p < 0.01$). VI from both PhenoCam and MODIS better predicted GPP (i.e., higher R^2) at longer time steps at all sites. The changes in the R^2 when using Landsat VI to predict GPP at different time steps were not consistent across sites. While there was an increase in R^2 from 8-day to longer time steps at both WKG and WHS, R^2 fluctuated across temporal scales at SRM. The sample reduction toward longer time steps due to temporal aggregation had little impact on these results (Supplemental Fig. S10). Similarly, using VI from ROIs with different view angles did not affect the R^2 variation across temporal scales. Specifically, the correlation coefficient between daily VI from mesquite ROI #1 and #7 was 0.87 while the correlation coefficient was 0.94 between daily VI from grass ROI #1 and #8. Moreover, the variation in R^2 across temporal scales calculated using footprint scale PhenoCam VI generated based on different combinations of the selected mesquite and grass ROIs was consistent with that in Fig. 8 (Supplemental Table S4). However, the R^2 for a given temporal scale did vary when the footprint scale PhenoCam VI generated based on different combinations of the selected mesquite and grass ROIs was used in the regression against GPP, and the variation can be as high as 0.12 (Table S4). This variation in R^2 indicates the view angle effects on the absolute VI values derived from PhenoCam imagery. For any given sensor at each site, Δ and RMSD exhibited decreases toward longer time steps with the exception being for Landsat at SRM (Supplemental Tables S5–S6).

5. Discussion

We systematically evaluated the changes in the VI-GPP relationship across spatiotemporal scales at three representative dryland sites in the southwestern United States. We found substantial changes in the greenness-GPP relationship across spatial scales only at the SRM savanna site. We also found that the relationship between greenness and GPP becomes stronger at longer time intervals with the best relationships observed at a monthly temporal resolution. In the following sections, we first explain the phenological differences between mesquite and grass, and how it affects seasonal GPP dynamics. We then discuss the differences in PhenoCam- and satellite-derived Phenology. We further discuss spatiotemporal scaling and why temporal aggregation strengthens the greenness-GPP relationship.

5.1. The differences between mesquite and grass phenology, and the differences between PhenoCam- and satellite-derived phenology

5.1.1. The phenological differences between mesquite and grass, and its relationship with GPP dynamics

The substantial differences in the greenness trajectories of mesquite and grass at the grassland site WKG and the savanna site SRM (Fig. 6a and b) can be explained by their very different leaf phenology. Mesquite in southeastern Arizona leaf out in early April, near the onset of the driest and hottest part of the year, and maintain these leaves until the occurrence of freezing events in late fall. A second flush of additional leaves can occur in abundant rainfall years during the monsoon. The perennial grass phenology, instead, is closely coupled to recent precipitation with more pulse-like greening occurring anytime from around February through September when temperatures are not limiting (Hamerlynck et al., 2012, 2010). However, significant spring greening of the grass is rare and limited in magnitude, and detection of grassland greening can be reduced by the previous summer season's brown leaves. Apparent increases of springtime grass greenness only occurred in 2015 at WKG and in 2016 at SRM (Fig. 6a and b). Browning et al. (2017) found that at least 25% of new growth in the grass canopy may be needed before PhenoCam can capture a change in greenness of a similar bunchgrass species. Thus, more limited springtime growth in these desert grasslands may not be captured by PhenoCam imagery.

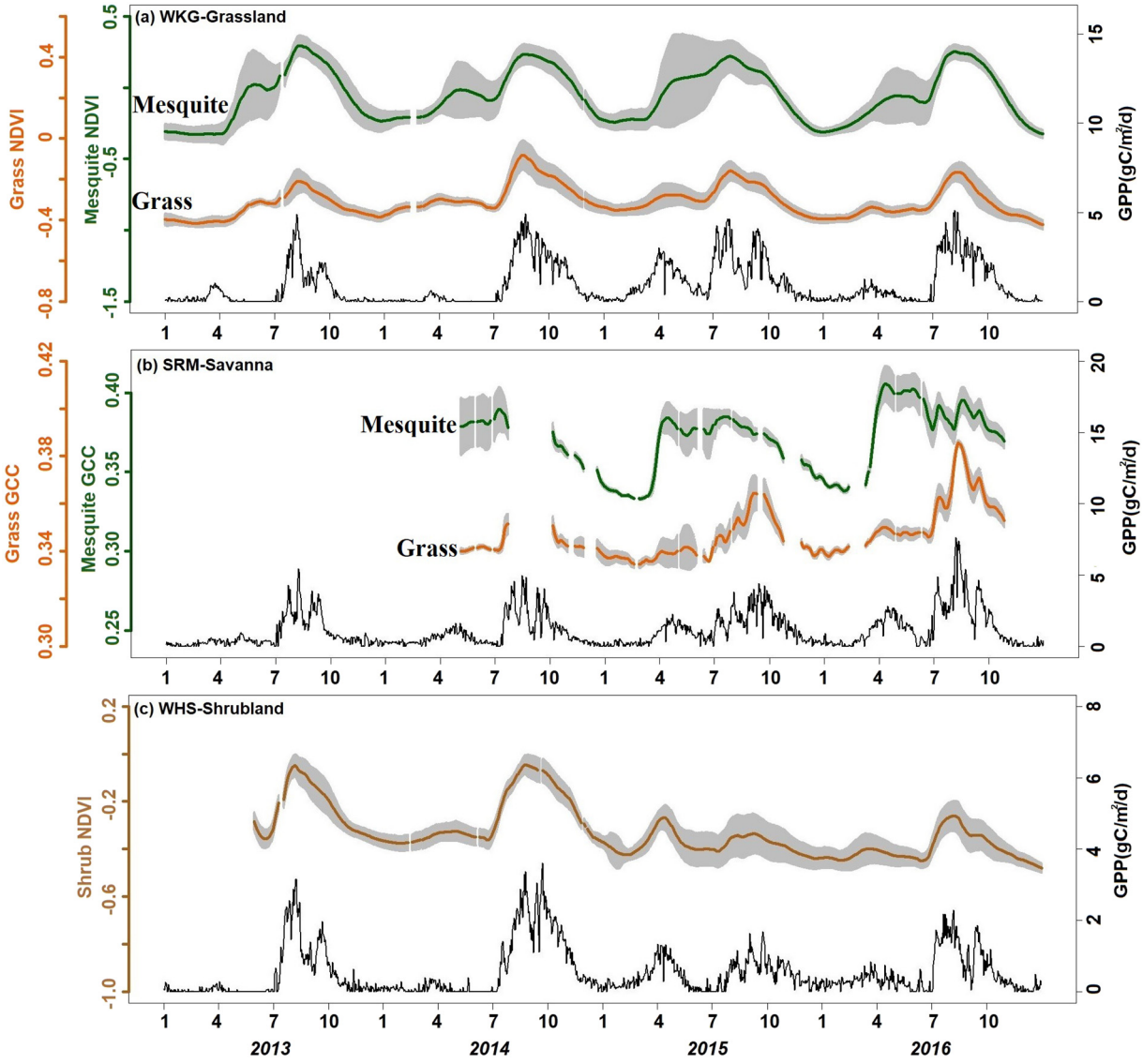

Fig. 6. The mean PhenoCam VI (left y-axis) extracted for major land cover types at the study sites. Note that GCC was calculated for the SRM site while NDVI was calculated at the WKG and WHS sites. The gray shade indicates one standard deviation above or below the mean VI. Tower GPP (right y-axis) is shown in black solid lines.

The relationship between greenness and GPP is also complicated by the soil moisture conservation strategy that mesquite trees utilize that can help sustain photosynthesis in the dryer periods of a year. For instance, at the SRM savanna site, while grasses mainly develop roots in the shallow soil layer, mesquite trees have both extensive lateral roots and deep tap roots (Scott et al., 2008). Results from previous studies indicate that the hydraulic redistribution of soil moisture by the roots of mesquite trees occur throughout the year, which benefit mesquite trees in the competition for soil moisture with understory grasses (Barron-Gafford et al., 2017; Scott et al., 2008). The spring GPP increase at SRM is primarily driven by the leaf emergence of mesquite trees in April (Fig. 6b). The spring GPP peak only lasts for a short time period since it is sustained by a limited amount of winter precipitation that has been redistributed by the tap roots in the deep soil profile (Scott et al., 2009, 2008). Mesquite trees maintain a relatively high level of greenness while GPP starts to decrease during late spring (Fig. 6b) due to strong stomatal control (Potts et al., 2008). The summer GPP increase is due to relaxed stomatal constraints on existing tree leaves and the greening and upregulation of the perennial grasses (Scott et al., 2009, 2008), the greenness of which is tightly coupled with GPP (Fig. 6b). Therefore, although mesquite shrubs at the SRM savanna site may flush additional leaves in summer, their greenness is not closely synchronized with ecosystem GPP (Fig. 6b). The hydraulic redistribution of soil moisture also occurs during the summer and it helps mesquite trees to maintain green leaves and sustain photosynthesis after the end of the monsoon season. This is likely why mesquite trees have a slower brown-down process than grasses (Fig. 6b) (Scott et al., 2009, 2008). Note that, there seemed to be a concurrent spring green-up of mesquite and grass on May 2nd, 2013 at the WKG grassland site, which occurred after the spring GPP peak. By carefully examining the PhenoCam imagery, we found that this was caused by a PhenoCam focus adjustment. We conducted an experiment by repeating the spatial and temporal regression analyses at the WKG site with the VI before May 2nd, 2013 excluded. Results from this experiment (Supplemental Table S7) indicate that the variations in R^2 across the spatial and temporal scales are consistent with our current results (Figs. 5a and 8a).

5.1.2. The differences between PhenoCam- and satellite-derived phenology

It is worth noting that there was a distinct delay in the phenology derived from satellite VI than that from PhenoCam VI during the senescence phase (i.e., months following the peak VI) at the WHS shrubland site (Fig. 4c). The delay in satellite-derived phenology during

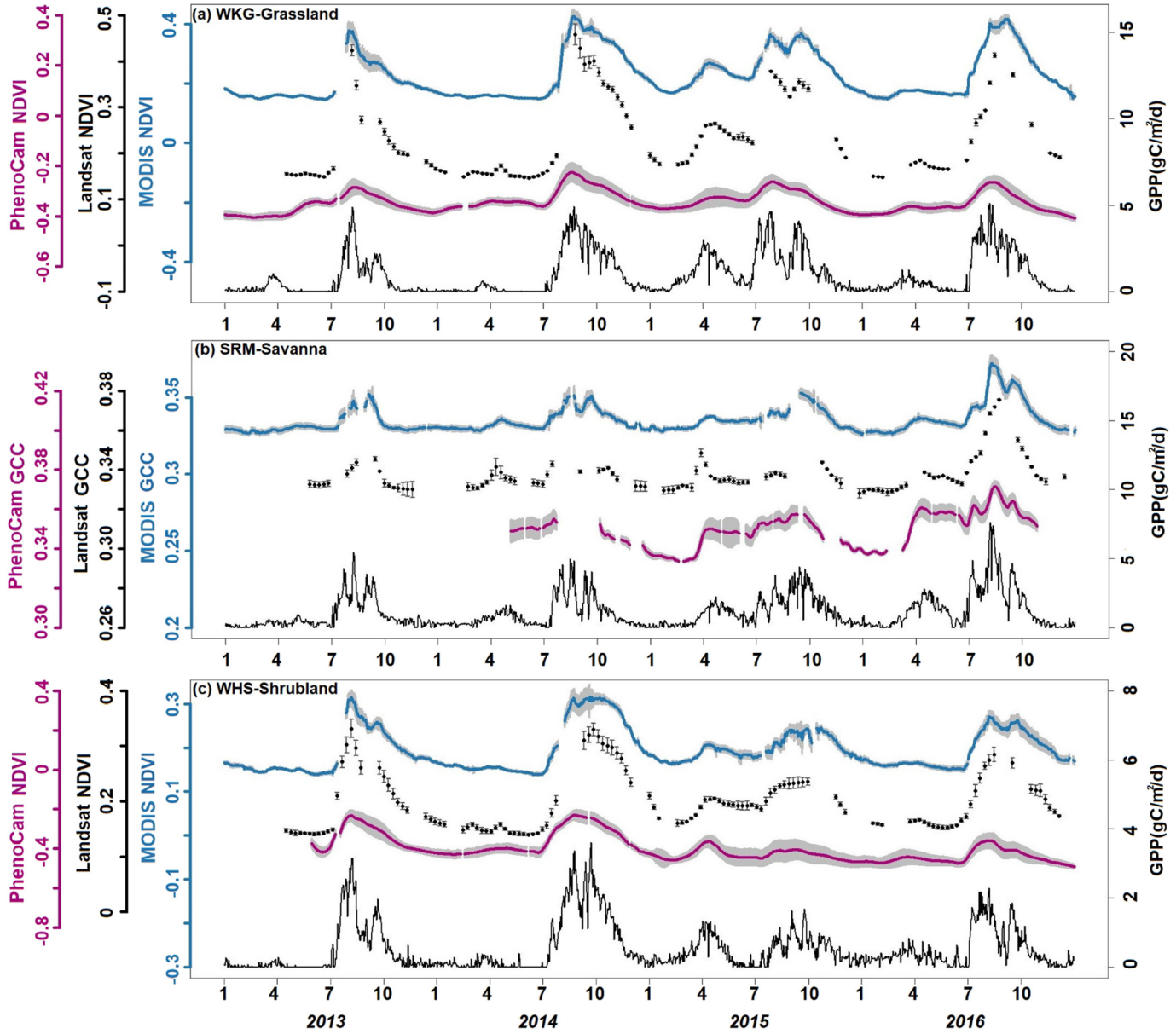

Fig. 7. The time series of tower footprint scale VI (the three y-axes on the left), and GPP (right y-axis) during 2013–2016 at the study sites. PhenoCam, Landsat and MODIS VI are shown in blue, black and purple, respectively. Note that GCC was calculated for the SRM site while NDVI was calculated at the WKG and WHS sites. The gray shaded area (i.e., PhenoCam and MODIS) and error bars (i.e., Landsat) indicate one standard deviation above or below the footprint scale VI. GPP is shown as solid black lines. (For interpretation of the references to color in this figure legend, the reader is referred to the web version of this article.)

the senescence phase has been explored in previous studies (Liu et al., 2017; Melaas et al., 2016; Zhang et al., 2018). As suggested by those studies, the delay is most likely caused by limited ability of satellite-derived VI to accurately monitor leaf phenology during the senescence phase. This is because, in contrast to the rapid leaf color change and leaf expansion during the green-up phase, the changes in leaf color and leaf area during the senescence phase are more gradual. Furthermore, there tends to be higher inter-species variability in the changes of leaf color and leaf area during the senescence phase. With a pixel size larger than the PhenoCam's field of view, it is possible that the satellite is seeing a more spatially variable thus slower process of greenness decreases than that observed by PhenoCam.

5.2. Greenness-GPP changes across spatial scales

At the SRM savanna site, the greenness of mesquite is decoupled from GPP during both late spring and summer (Fig. 6b). In contrast, the greenness of grass is tightly coupled with GPP during summer, which represents the major growing season. Since PhenoCam imagery was captured from an oblique angle, grass and bare soil can mainly be seen in the foreground whereas they were blocked by the canopy of mesquite trees in areas further away from the camera within the PhenoCam's field-of-view at the SRM site (Fig. 3b). This is another piece of evidence demonstrating the view angle effects in PhenoCam VI. As a result, the PhenoCam ROI was dominated by mesquite trees (Fig. 3b and S1d) whereas grass was the dominant land cover at the scale of Landsat and MODIS (Fig. S2a), which captured imagery from a more nadir angle. Therefore, the difference in the correlation with GPP between the greenness of mesquite and grass along with the change in the dominant land cover resulted in the substantial changes in the strength of greenness-GPP relationship across spatial scales. At the grassland site WKG, the R^2 was consistent across spatial scale, because grass was the dominant land cover across spatial scales and its greenness is closely coupled with GPP (Figs. 5d and 6a). Although the dominant land cover

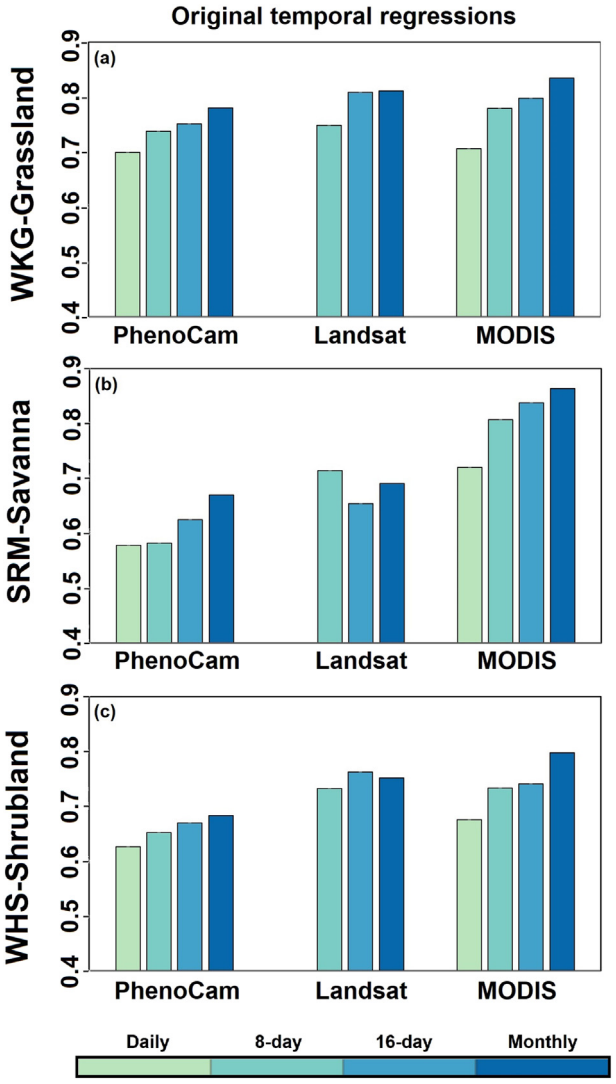

Fig. 8. Coefficients of determination (R^2) for VI-GPP relationship over changes in temporal scales.

was not consistent across spatial scales at the shrubland site WHS (Fig. 5i), the R^2 remained relatively consistent because shrub is the only land cover type with photosynthetic capacity. The increase in R^2 at the SRM savanna site was probably not caused by the differences in viewing geometry between PhenoCam and satellites because it did not affect the R^2 values at the other two study sites.

5.3. Greenness-GPP changes across temporal scales

We found stronger greenness-GPP relationships when both greenness and GPP were averaged over longer temporal intervals (Fig. 8). This is because averaging removes the high short-term variability in GPP, associated with fast-changing environmental conditions, that is not captured by greenness (Sims et al., 2006b). In Fig. 7 for example, it is obvious that the day-to-day variability in GPP is much higher than that in VI. This is because GPP is affected by photosynthetically active radiation and other hydrometeorological conditions (e.g., humidity, temperature, soil moisture), which vary at sub-daily scales and affect leaf level gas exchange (Running et al., 2004; Sims et al., 2006b). In contrast, greenness is mediated by leaf chlorophyll content and canopy structure (Carlson and Ripley, 1997; Gitelson and Merzlyak, 1997), which vary slower than the hydrometeorological conditions and associated plant gas exchange regulation (Supplemental Fig. S11). This finding appears consistent across the study sites included in this study (Fig. 8). The one exception was observed between GPP and Landsat VI at the SRM savanna site. We suggest that outliers in the Landsat VI time series likely caused this exception. Specifically, Supplemental Fig. S6 presents the comparison of tower footprint scale Landsat and MODIS VI. VI from Landsat and MODIS have strong agreements at the WKG and WHS sites with a correlation coefficient of 0.99 and 0.98, respectively. In contrast, Landsat and MODIS VI have relatively weak agreement at the SRM savanna site with a correlation coefficient of 0.89. We suspect that the relatively weak agreement at the SRM site was caused by outliers in Landsat VI (i.e., Fig. S6b). These outliers not only exhibited abrupt changes when compared to neighboring Landsat VI but also were much higher than the concurrent MODIS VI. When we repeated the regression analyses between Landsat VI and GPP at the SRM site with these outliers excluded, we found that the R^2 between VI and GPP at 8-day, 16-day and monthly scale increased to 0.75, 0.76 and 0.73, respectively (in contrast to the R^2 of 0.71, 0.65 and 0.69 at the corresponding time scales in Fig. 8b). Further, the variation in R^2 became more consistent with the patterns observed at the WKG and WHS sites (Fig. 8a and c). Since outliers in Landsat VI time series were mainly found at the SRM site, the conditions that resulted in these outliers are worth being investigated in future studies. We point out that the R^2 between Landsat VI and GPP at a given spatial or temporal scale might also be affected by missing Landsat VI during particular phenological periods as a result of its relatively low temporal resolution. However, the experiment design of this study should provide sufficient sampling of VI-GPP relationship during different phenological periods. Specifically, we used Landsat VI from multiple years, the missing Landsat VI during a particular phenological period in one year may become available during same phenological period of another year (Figs. 4 and 7). In addition, we also used daily VI time series of PhenoCam and MODIS to study changes in VI-GPP relationship. Based on the VI availability demonstrated in Figs. 4 and 7, it is evident that VI from either PhenoCam or MODIS could cover the phenological periods during which Landsat VI was continuously missing during the entire study period.

Our results highlight the needs for alternative remote sensing proxies of short-term GPP changes in drylands. Solar-induced-fluorescence (SIF) has been found to outperform the Enhanced Vegetation Index in terms of tracking GPP dynamics across the drylands of southwestern North America (Smith et al., 2018). The recently launched TROPOspheric Monitoring Instrument (TROPOMI) provides global SIF measurement on a daily basis thus holds great potential to reduce the uncertainty in tracking dryland GPP dynamics at short temporal intervals (Guanter et al., 2015). Results from previous studies have also shown that the pigment-based Photochemical Reflectance Index (PRI) (Gamon et al., 1992) and water-content-based Water Band Index (WBI) (Penuelas et al., 1997) are also very useful in monitoring productivity-related traits of dryland plants. For example, PRI has been shown to be very useful in estimating leaf pigment content of a wide range of dryland plant species (Sims and Gamon, 2002), and monitoring light use efficiency in a chaparral ecosystem (Sims et al., 2006a). WBI has been found to have better performance in the detection of plant biophysical properties (e.g., water content and biomass) in a semi-arid grassland ecosystem than that of NDVI (Rahman and Gamon, 2004). The Fluorescence Imaging Spectrometer (FLORIS), which will be onboard the upcoming Fluorescence Explorer Mission of the European Space Agency (scheduled for launch in 2022), is able to provide coupled SIF and PRI measurements with a spatial resolution of about 300 m, and thus another promising instrument in improving dryland GPP monitoring (Drusch et al., 2017; Kraft et al., 2013). We also point out that our analysis was based on a static relative percent cover of key plant functional types (e.g., mesquite, grass, shrub). The land cover data with higher spatiotemporal resolution that better captures seasonal shifts in relative percent cover of key plant functional types may also enable improved GPP estimates using PhenoCam VI in dryland ecosystems.

6. Conclusions

The results from our study show that VI-GPP relationships are mediated by different factors in the spatial and temporal domains. In the spatial domain, the usefulness of using VI to track GPP changes decreases when land cover heterogeneity is high. In the temporal domain, the relationship between VI and GPP becomes stronger at longer time intervals with the best relationships observed at a monthly temporal resolution. The reason the VI-GPP relationship breaks down at short timescales is most likely because VIs vary at a much lower frequency relative to GPP. Therefore, we recommend cautious interpretation of VI-derived GPP dynamics at relatively short temporal intervals, especially for dryland ecosystem types.

Acknowledgements

This work is supported by a contract from the Strategic Environmental Research and Development Program (SERDP; project number RC18-1322) and the United States Department of Agriculture (USDA; cooperative agreement number 58-0111-17-013). We also acknowledge the support for this work provided by the United States Department of Energy (DOE; Regional and Global Climate Modeling DE-SC0016011) and DOE's Ameriflux Management Program. The development of PhenoCam has been supported by the Northeastern States Research Cooperative, NSF's Macrosystems Biology Program (awards EF-1065029 and EF-1702697), DOE's Regional and Global Climate Modeling program (award DE-SC0016011), the US National Park Service Inventory and Monitoring Program and the USA National Phenology Network (grant number G10AP00129 from the United States Geological Survey), and the USA National Phenology Network and the North Central Climate Science Center (cooperative agreement number G16AC00224 from the United States Geological Survey). PhenoCam collaborators, including site PIs and technicians, are thanked for their efforts in support of PhenoCam. Research at Walnut Gulch Watershed and the Santa Rita Range is supported by the USDA Agricultural Research Service and University of Arizona. We thank Leland Sutter at the University of Arizona for his help with the manuscript revision.

Appendix A. Supplementary data

Supplementary data to this article can be found online at https://doi.org/10.1016/j.rse.2018.12.029.

References

Ahlström, A., Raupach, M.R., Schurgers, G., Smith, B., Arneth, A., Jung, M., Reichstein, M., Canadell, J.G., Friedlingstein, P., Jain, a.K., Kato, E., Poulter, B., Sitch, S., Stocker, B.D., Viovy, N., Wang, Y.P., Wiltshire, A., Zaehle, S., Zeng, N., 2015. The dominant role of semi-arid ecosystems in the trend and variability of the land CO2 sink. Science (80-.) 348, 895–899. https://doi.org/10.1126/science.aaa1668.

Archer, S., Boutton, T.W., Hibbard, K.A., 2001. 1.9 - Trees in Grasslands: Biogeochemical Consequences of Woody Plant Expansion BT - Global Biogeochemical Cycles in the Climate System. Academic Press, San Diego, pp. 115–137. https://doi.org/10.1016/B978-012631260-7/50011-X.

Barnes, M.L., Breshears, D.D., Law, D.J., van Leeuwen, W.J.D., Monson, R.K., Fojtik, A.C., Barron-Gafford, G.A., Moore, D.J.P., 2017. Beyond greenness: detecting temporal changes in photosynthetic capacity with hyperspectral reflectance data. PLoS One 12, e0189539.

Barron-Gafford, G.A., Sanchez-Cañete, E.P., Minor, R.L., Hendryx, S.M., Lee, E., Sutter, L.F., Tran, N., Parra, E., Colella, T., Murphy, P.C., Hamerlynck, E.P., Kumar, P., Scott, R.L., 2017. Impacts of hydraulic redistribution on grass–tree competition vs facilitation in a semi-arid savanna. New Phytol. 215, 1451–1461. https://doi.org/10.1111/nph.14693.

Biederman, J.A., Scott, R.L., Bell, T.W., Bowling, D.R., Dore, S., Garatuza-Payan, J., Kolb, T.E., Krishnan, P., Krofcheck, D.J., Litvak, M.E., Maurer, G.E., Meyers, T.P., Oechel, W.C., Papuga, S.A., Ponce-Campos, G.E., Rodriguez, J.C., Smith, W.K., Vargas, R., Watts, C.J., Yepez, E.A., Goulden, M.L., 2017. CO2 exchange and evapotranspiration across dryland ecosystems of southwestern North America. Glob. Chang. Biol. 23, 4204–4221. https://doi.org/10.1111/gcb.13686.

Biederman, J.A., Scott, R.L., Arnone, J.A., Jasoni, R.L., Litvak, M.E., Moreo, M.T., Papuga, S.A., Ponce-Campos, G.E., Schreiner-McGraw, A.P., Vivoni, E.R., 2018. Shrubland carbon sink depends upon winter water availability in the warm deserts of North America. Agric. For. Meteorol. 249, 407–419. https://doi.org/10.1016/j.agrformet.2017.11.005.

Browning, D.M., Karl, J.W., Morin, D., Richardson, A.D., Tweedie, C.E., 2017. Phenocams bridge the gap between field and satellite observations in an arid grassland. Remote Sens. https://doi.org/10.3390/rs9101071. (in review).

Broxton, P.D., Zeng, X., Sulla-Menashe, D., Troch, P.A., 2014. A global land cover climatology using MODIS data. J. Appl. Meteorol. Climatol. 53, 1593–1605. https://doi.org/10.1175/JAMC-D-13-0270.1.

Carlson, T.N., Ripley, D.A., 1997. On the relation between NDVI, fractional vegetation cover, and leaf area index. Remote Sens. Environ. 62, 241–252. https://doi.org/10.1016/S0034-4257(97)00104-1.

Derner, J.D., Schuman, G.E., 2007. Carbon sequestration and rangelands: a synthesis of land management and precipitation effects. J. Soil Water Conserv. 62, 77–85. https://doi.org/10.1006/anbo.1999.0829.

Drusch, M., Moreno, J., Del Bello, U., Franco, R., Goulas, Y., Huth, A., Kraft, S., Middleton, E.M., Miglietta, F., Mohammed, G., Nedbal, L., Rascher, U., Schüttemeyer, D., Verhoef, W., 2017. ESA's water mission ESA's Earth explorer missions. Atlantica 55, 1273–1284.

Filippa, G., Cremonese, E., Migliavacca, M., Galvagno, M., Forkel, M., Wingate, L., Tomelleri, E., Morra di Cella, U., Richardson, A.D., 2016. Phenopix: a R package for image-based vegetation phenology. Agric. For. Meteorol. 220, 141–150. https://doi.org/10.1016/j.agrformet.2016.01.006.

Filippa, G., Cremonese, E., Migliavacca, M., Galvagno, M., Sonnentag, O., Humphreys, E., Hufkens, K., Ryu, Y., Verfaillie, J., Morra di Cella, U., Richardson, A.D., 2018. NDVI derived from near-infrared-enabled digital cameras: applicability across different plant functional types. Agric. For. Meteorol. 249, 275–285. https://doi.org/10.1016/j.agrformet.2017.11.003.

Frankenberg, Fisher, J.B., Worden, J., Badgley, G., Saatchi, S.S., Lee, J.E., Toon, G.C., Butz, A., Jung, M., Kuze, A., Yokota, T., 2011. New global observations of the terrestrial carbon cycle from GOSAT: patterns of plant fluorescence with gross primary productivity. Geophys. Res. Lett. 38. https://doi.org/10.1029/2011GL048738.

Gamon, J.A., 2015. Reviews and syntheses: optical sampling of the flux tower footprint. Biogeosciences 12, 4509–4523. https://doi.org/10.5194/bg-12-4509-2015.

Gamon, J.A., Peñuelas, J., Field, C.B., 1992. A narrow-waveband spectral index that tracks diurnal changes in photosynthetic efficiency. Remote Sens. Environ. 41, 35–44. https://doi.org/10.1016/0034-4257(92)90059-S.

Gitelson, A.A., Merzlyak, M.N., 1997. Remote estimation of chlorophyll content in higher plant leaves. Int. J. Remote Sens. 18, 2691–2697. https://doi.org/10.1080/014311697217558.

Guanter, L., Aben, I., Tol, P., Krijger, J.M., Hollstein, A., Köhler, P., Damm, A., Joiner, J., Frankenberg, C., Landgraf, J., 2015. Potential of the TROPOspheric Monitoring Instrument (TROPOMI) onboard the Sentinel-5 Precursor for the monitoring of terrestrial chlorophyll fluorescence. Atmos. Meas. Tech. 8, 1337–1352. https://doi.org/10.5194/amt-8-1337-2015.

Hamerlynck, E.P., Scott, R.L., Moran, M.S., Keefer, T.O., Huxman, T.E., 2010. Growing season ecosystem and leaf-level gas exchange of an exotic and native semiarid bunchgrass. Oecologia 163, 561–570. https://doi.org/10.1007/s00442-009-1560-1.

Hamerlynck, E.P., Scott, R.L., Barron-Gafford, G.A., Cavanaugh, M.L., Susan Moran, M., Huxman, T.E., 2012. Cool-season whole-plant gas exchange of exotic and native semiarid bunchgrasses. Plant Ecol. 1–11. https://doi.org/10.1007/s11258-012-0081-x.

Hewins, D.B., Lyseng, M.P., Schoderbek, D.F., Alexander, M., Willms, W.D., Carlyle, C.N., Chang, S.X., Bork, E.W., 2018. Grazing and climate effects on soil organic carbon concentration and particle-size association in northern grasslands. Sci. Rep. 8, 1336. https://doi.org/10.1038/s41598-018-19785-1.

Hufkens, K., Friedl, M., Sonnentag, O., Braswell, B.H., Milliman, T., Richardson, A.D., 2012. Linking near-surface and satellite remote sensing measurements of deciduous broadleaf forest phenology. Remote Sens. Environ. 117, 307–321. https://doi.org/10.1016/j.rse.2011.10.006.

Jung, M., Reichstein, M., Schwalm, C.R., Huntingford, C., Sitch, S., Ahlström, A., Arneth, A., Camps-Valls, G., Ciais, P., Friedlingstein, P., Gans, F., Ichii, K., Jain, A.K., Kato, E., Papale, D., Poulter, B., Raduly, B., Rödenbeck, C., Tramontana, G., Viovy, N., Wang, Y.-P., Weber, U., Zaehle, S., Zeng, N., 2017. Compensatory water effects link yearly global land CO2 sink changes to temperature. Nature 541, 516–520.

Kraft, S., Bézy, J.-L., Del Bello, U., Berlich, R., Drusch, M., Franco, R., Gabriele, A., Harnisch, B., Meynart, R., Silvestrin, P., 2013. FLORIS: Phase A Status of the Fluorescence Imaging Spectrometer of the Earth Explorer Mission Candidate FLEX 88890T. https://doi.org/10.1117/12.2032060.

Liu, Y., Hill, M.J., Zhang, X., Wang, Z., Richardson, A.D., Hufkens, K., Filippa, G., Baldocchi, D.D., Ma, S., Verfaillie, J., Schaaf, C.B., 2017. Using data from Landsat, MODIS, VIIRS and PhenoCams to monitor the phenology of California oak/grass savanna and open grassland across spatial scales. Agric. For. Meteorol. 237–238, 311–325. https://doi.org/10.1016/j.agrformet.2017.02.026.

Melaas, E.K., Sulla-Menashe, D., Gray, J.M., Black, T.A., Morin, T.H., Richardson, A.D., Friedl, M.A., 2016. Multisite analysis of land surface phenology in North American temperate and boreal deciduous forests from Landsat. Remote Sens. Environ. 186, 452–464. https://doi.org/10.1016/j.rse.2016.09.014.

Milliman, T., Hufkens, K., Richardson, A.D., Aubrecht, D.M., Chen, M., Gray, J.M., Johnston, M.R., Keenan, T., Klosterman, S.T., Kosmala, M., Melaas, E.K., Friedl, M.A., Frolking, S., Abraha, M., Alber, M., Apple, M., Law, B.E., Black, T.A., Blanken, P., Browning, D., Bret-Harte, S., Brunsell, N., Burns, S.P., Cremonese, E., Desai, A.R., Dunn, A.L., Eissenstat, D.M., Euskirchen, S.E., Flanagan, L.B., Forsythe, B., Gallagher, J., Gu, L., Hollinger, D.Y., Jones, J.W., King, J., Langvall, O., McCaughey, J.H., McHale, P.J., Meyer, G.A., Mitchell, M.J., Migliavacca, M., Nesic, Z., Noormets, A., Novick, K., O'Connell, J., Oishi, A.C., Oswald, W.W., Perkins, T.D., Phillips, R.P., Schwartz, M.D., Scott, R.L., Sonnentag, O., Thom, J.E., 2018. PhenoCam Dataset

v1.0: Digital Camera Imagery From the PhenoCam Network, 2000–2015. https://doi.org/10.3334/ornldaac/1560.
Monteith, J.L., 1972. Solar radiation and productivity in tropical ecosystems. J. Appl. Ecol. 9, 747–766. https://doi.org/10.2307/2401901.
O. DAAC, 2017. MODIS Collection 6 Land Products Global Subsetting and Visualization Tool. Subset Obtained for MOD13Q1.006 Product, Time Period: 01 January 2006 to 31 December 2016. https://doi.org/10.3334/ORNLDAAC/1379.
Pacala, S.W., Hurtt, G.C., Baker, D., Peylin, P., Houghton, R.A., Birdsey, R.A., Heath, L., Sundquist, E.T., Stallard, R.F., Ciais, P., Moorcroft, P., Caspersen, J.P., Shevliakova, E., Moore, B., Kohlmaier, G., Holland, E., Gloor, M., Harmon, M.E., Fan, S.-M., Sarmiento, J.L., Goodale, C.L., Schimel, D., Field, C.B., 2001. Consistent land- and atmosphere-based U.S. carbon sink estimates. Science (80-.) 292, 2316–2320.
Penuelas, J., Pinol, J., Ogaya, R., Filella, I., 1997. Estimation of plant water concentration by the reflectance Water Index WI (R900/R970). Int. J. Remote Sens. 18, 2869–2875. https://doi.org/10.1080/014311697217396.
Petach, A.R., Toomey, M., Aubrecht, D.M., Richardson, A.D., 2014. Monitoring vegetation phenology using an infrared-enabled security camera. Agric. For. Meteorol. 195, 143–151. https://doi.org/10.1016/j.agrformet.2014.05.008.
Potts, D.L., Scott, R.L., Cable, J.M., Huxman, T.E., Williams, D.G., 2008. Sensitivity of mesquite shrubland CO2 exchange to precipitation in contrasting landscape settings. Ecology 89, 2900–2910. https://doi.org/10.1890/07-1177.1.
Rahman, A.F., Gamon, J.A., 2004. Detecting biophysical properties of a semi-arid grassland and distinguishing burned from unburned areas with hyperspectral reflectance. J. Arid Environ. 58, 597–610. https://doi.org/10.1016/j.jaridenv.2003.12.005.
Rahman, A.F., Sims, D.A., Cordova, V.D., El-Masri, B.Z., 2005. Potential of MODIS EVI and surface temperature for directly estimating per-pixel ecosystem C fluxes. Geophys. Res. Lett. 32, 1–4. https://doi.org/10.1029/2005GL024127.
Reynolds, J.F., Smith, D.M.S., Lambin, E.F., Turner, B.L., Mortimore, M., Batterbury, S.P.J., Downing, T.E., Dowlatabadi, H., Fernández, R.J., Herrick, J.E., Huber-Sannwald, E., Jiang, H., Leemans, R., Lynam, T., Maestre, F.T., Ayarza, M., Walker, B., 2007. Global desertification: building a science for dryland development. Science (80-.) 316, 847–851.
Richardson, A.D., Hufkens, K., Milliman, T., Aubrecht, D.M., Chen, M., Gray, J.M., Johnston, M.R., Keenan, T.F., Klosterman, S.T., Kosmala, M., Melaas, E.K., Friedl, M.A., Frolking, S., 2018. Tracking vegetation phenology across diverse North American biomes using PhenoCam imagery. Sci. Data 5, 180028.
Running, S.W., Nemani, R.R., Heinsch, F.A., Zhao, M., Reeves, M., Hashimoto, H., 2004. A continuous satellite-derived measure of global terrestrial primary production. Bioscience 54, 547. https://doi.org/10.1641/0006-3568(2004)054[0547:ACSMOG]2.0.CO;2.
Schaaf, C., Wang, Z., 2015. MCD43A4 MODIS/Terra + Aqua BRDF/Albedo Nadir BRDF Adjusted RefDaily L3 Global - 500m V006. NASA EOSDIS Land Processes DAAChttps://doi.org/10.5067/MODIS/MCD43A4.006.
Schmid, H.P., 2002. Footprint modeling for vegetation atmosphere exchange studies: a review and perspective. Agric. For. Meteorol. 113, 159–183. https://doi.org/10.1016/S0168-1923(02)00107-7.
Scott, R.L., 2010. Using watershed water balance to evaluate the accuracy of eddy covariance evaporation measurements for three semiarid ecosystems. Agric. For. Meteorol. 150, 219–225. https://doi.org/10.1016/j.agrformet.2009.11.002.
Scott, Huxman, T.E., Williams, D.G., Goodrich, D.C., 2006a. Ecohydrological impacts of woody-plant encroachment: seasonal patterns of water and carbon dioxide exchange within a semiarid riparian environment. Glob. Chang. Biol. 12, 311–324. https://doi.org/10.1111/j.1365-2486.2005.01093.x.
Scott, R.L., Huxman, T.E., Cable, W.L., Emmerich, W.E., 2006b. Partitioning of evapotranspiration and its relation to carbon dioxide exchange in a Chihuahuan Desert shrubland. Hydrol. Process. 20, 3227–3243. https://doi.org/10.1002/hyp.6329.
Scott, R.L., Cable, W.L., Hultine, K.R., 2008. The ecohydrologic significance of hydraulic redistribution in a semiarid savanna. Water Resour. Res. 44. https://doi.org/10.1029/2007WR006149.
Scott, R.L., Jenerette, G.D., Potts, D.L., Huxman, T.E., 2009. Effects of seasonal drought on net carbon dioxide exchange from a woody-plant-encroached semiarid grassland. J. Geophys. Res. Biogeosci. 114. https://doi.org/10.1029/2008JG000900.
Scott, R.L., Hamerlynck, E.P., Jenerette, G.D., Moran, M.S., Barron-Gafford, G.A., 2010. Carbon dioxide exchange in a semidesert grassland through drought-induced vegetation change. J. Geophys. Res. Biogeosci. 115, 1–12. https://doi.org/10.1029/2010JG001348.
Scott, R.L., Biederman, J.A., Hamerlynck, E.P., Barron-Gafford, G.A., 2015. The carbon balance pivot point of southwestern U.S. semiarid ecosystems: insights from the 21st century drought. J. Geophys. Res. Biogeosci. 120, 2612–2624. https://doi.org/10.1002/2015JG003181.
Sims, D.A., Gamon, J.A., 2002. Relationships between leaf pigment content and spectral reflectance across a wide range of species, leaf structures and developmental stages. Remote Sens. Environ. 81, 337–354. https://doi.org/10.1016/S0034-4257(02)00010-X.
Sims, D.A., Luo, H., Hastings, S., Oechel, W.C., Rahman, A.F., Gamon, J.A., 2006a. Parallel adjustments in vegetation greenness and ecosystem CO2 exchange in response to drought in a Southern California chaparral ecosystem. Remote Sens. Environ. 103, 289–303. https://doi.org/10.1016/j.rse.2005.01.020.
Sims, D.A., Rahman, A.F., Cordova, V.D., El-Masri, B.Z., Baldocchi, D.D., Flanagan, L.B., Goldstein, A.H., Hollinger, D.Y., Misson, L., Monson, R.K., Oechel, W.C., Schmid, H.P., Wofsy, S.C., Xu, L., 2006b. On the use of MODIS EVI to assess gross primary productivity of North American ecosystems. J. Geophys. Res. Biogeosci. 111, 1–16. https://doi.org/10.1029/2006JG000162.
Smith, W. k, Reed, S.C., Cleveland, C.C., Ballantyne, A.P., Anderegg, W.R.L., Wieder, W.R., Liu, Y.Y., Running, S.W., 2016. Large divergence of satellite and Earth system model estimates of global terrestrial CO2 fertilization. Nat. Clim. Chang. 6, 306–310.
Smith, W.K., Biederman, J.A., Scott, R.L., Moore, D.J.P., He, M., Kimball, J.S., Yan, D., Hudson, A., Barnes, M.L., Macbean, N., Fox, A., Litvak, M.E., 2018. Chlorophyll fluorescence better captures seasonal and interannual gross primary productivity dynamics across dryland ecosystems of southwestern North America. Geophys. Res. Lett. https://doi.org/10.1002/2017GL075922.
Sonnentag, O., Hufkens, K., Teshera-Sterne, C., Young, A.M., Friedl, M., Braswell, B.H., Milliman, T., O'Keefe, J., Richardson, A.D., 2012. Digital repeat photography for phenological research in forest ecosystems. Agric. For. Meteorol. 152, 159–177. https://doi.org/10.1016/j.agrformet.2011.09.009.
Tian, Y., Romanov, P., Yu, Y., Xu, H., Tarpley, D., 2010. Analysis of vegetation index NDVI anisotropy to improve the accuracy of the GOES-R Green Vegetation Fraction product. In: Int. Geosci. Remote Sens. Symp. pp. 2091–2094. https://doi.org/10.1109/IGARSS.2010.5651925.
Toomey, M., Friedl, M.A., Frolking, S., Hufkens, K., Klosterman, S., Sonnentag, O., Baldocchi, D.D., Bernacchi, C.J., Biraud, S.C., Bohrer, G., Brzostek, E., Burns, S.P., Coursolle, C., Hollinger, D.Y., Margolis, H.A., McCaughey, H., Monson, R.K., Munger, J.W., Pallardy, S., Phillips, R.P., Torn, M.S., Wharton, S., Zeri, M., Richardson, A.D., 2015. Greenness indices from digital cameras predict the timing and seasonal dynamics of canopy-scale photosynthesis. Ecol. Appl. 25, 99–115. https://doi.org/10.1890/14-0005.1.
Verma, M., Friedl, M.A., Richardson, A.D., Kiely, G., Cescatti, A., Law, B.E., Wohlfahrt, G., Gielen, B., Roupsard, O., Moors, E.J., Toscano, P., Vaccari, F.P., Gianelle, D., Bohrer, G., Varlagin, A., Buchmann, N., van Gorsel, E., Montagnani, L., Propastin, P., 2014. Remote sensing of annual terrestrial gross primary productivity from MODIS: an assessment using the FLUXNET La Thuile data set. Biogeosciences 11, 2185–2200. https://doi.org/10.5194/bg-11-2185-2014.
Wylie, B.K., Johnson, D.A., Laca, E., Saliendra, N.Z., Gilmanov, T.G., Reed, B.C., Tieszen, L.L., Worstell, B.B., 2003. Calibration of remotely sensed, coarse resolution NDVI to CO2fluxes in a sagebrush-steppe ecosystem. Remote Sens. Environ. 85, 243–255. https://doi.org/10.1016/S0034-4257(03)00004-X.
Zhang, X., Jayavelu, S., Liu, L., Friedl, M.A., Henebry, G.M., Liu, Y., Schaaf, C.B., Richardson, A.D., Gray, J., 2018. Evaluation of land surface phenology from VIIRS data using time series of PhenoCam imagery. Agric. For. Meteorol. 256–257, 137–149. https://doi.org/10.1016/j.agrformet.2018.03.003.
Zhao, M., Heinsch, F.A., Nemani, R.R., Running, S.W., 2005. Improvements of the MODIS terrestrial gross and net primary production global data set. Remote Sens. Environ. 95, 164–176. https://doi.org/10.1016/j.rse.2004.12.011.